Journal Name

ARTICLE

Unique walnut-shaped porous MnO_2/C nanospheres with enhanced reaction kinetics for lithium storage with high capacity and superior rate capability

Received 00th January 20xx,
Accepted 00th January 20xx

DOI: 10.1039/x0xx00000x

www.rsc.org/

Shao-Zhuan Huang,[a] Yi Cai,[a] Jun Jin,[a] Jing Liu,[a] Yu Li,*[,a] Hong-En Wang,[a] Li-Hua Chen,[a] Tawfique Hasan[b] and Bao-Lian Su*[,a,c,d]

Unique walnut-shaped porous MnO_2/carbon nanospheres (P-MO/C-NSs) with high monodispersity have been designed and prepared for lithium storage via *in situ* carbonization of amorphous MnO_2 nanospheres. Polyvinylpyrrolidone (PVP) is utilized as both the surfactant for morphology control and carbon source for carbon scaffold formation accompanying with MnO_2 crystallization. Such unique walnut-shaped porous nanostructure with intimate carbon layer provides a large contact area with electrolyte, short transport path length for Li^+, low resistance for charge transfer and superior structural stability. The P-MO/C-NS electrode demonstrates high lithium storage capacity (1176 mA h g^{-1} at 100 mA g^{-1}), very good cycling stability (100% capacity retention versus the second cycle) and excellent rate capability (540 mA h g^{-1} at 1000 mA g^{-1}). We propose that it is the deep oxidation of Mn^{2+} to Mn^{3+} in P-MO/C-NSs resulting in an extraordinarily high capacity of 1192 mA h g^{-1} at a current density of 1000 mA g^{-1} after a long period of cycling, very close to the maximum theoretical reversible capacity of MnO_2 (1230 mA h g^{-1}). This is the highest value observed for MnO_2-based electrodes. The high lithium storage capacity and rate capability can be attributed to the enhanced reaction kinetics owing to the walnut-shaped porous nanostructure with intimate carbon layer. This work provides a meaningful demonstration of designing porous nanostructures of carbon-coated metal oxides undergoing deep conversion reactions for enhanced electrochemical performances.

1. Introduction

To develop next-generation lithium-ion batteries (LIBs) with high power and energy densities, nanotechnology has become one of the key approaches to realize novel electrode materials with high electrochemical performance.[1-3] Indeed, many nanostructured metal oxides, such as CoO_x, MnO_x, FeO_x have attracted great interest as potential high performance anode materials because of their significantly higher theoretical specific capacities and safer nature than those of the commercial carbon-based anode materials.[4-8]

As a typical metal oxide, manganese dioxide (α-MnO_2), containing 2×2 tunnels constructed from double chains of octahedral [MnO_6] structure, has been extensively studied as an anodic electrode for LIBs due to its high storage capacity, low cost, low toxicity and natural abundance.[9, 10] However, poor electrical conductivity and large volume expansion during the cycling process of this material result in poor cyclability and rate capability, severely restricting its practical utilization in LIBs.

To date, several strategies have been pursued to improve the cyclability and rate capability of MnO_2. The most widely used method involves coating MnO_2 with conductive carbon materials, which can enhance the electrical conductivity and buffer the volume expansion/contraction upon cycling.[10-12] An enhanced lithium storage process not only requires good electrical conductivity but also shortened lithium transport pathway. In this context, synthesizing electrode materials in nanoscale offers an effective method to decrease the diffusion length of electrons and lithium ions and improve the electrochemical activity of electrode materials.[13-15] Additionally, introducing porosity in nanostructure can not only increase surface area for contact between electrode and electrolyte, but also provide more space for the volume change during cycling, enhancing lithium ion diffusion kinetics.[16, 17] Thus, integrating the abovementioned three strategies in one MnO_2 nanostructure is expected to offer significant electrochemical property enhancement. Although various preparation methods, such as ultrafiltration

[a] *Laboratory of Living Materials at the State Key Laboratory of Advanced Technology for Materials Synthesis and Processing, Wuhan University of Technology, 122 Luoshi Road, 430070 Wuhan, Hubei, China; Email: yu.li@whut.edu.cn and baoliansu@whut.edu.cn*
[b] *Cambridge Graphene Centre, University of Cambridge, Cambridge, CB3 0FA, United Kingdom.*
[c] *Laboratory of Inorganic Materials Chemistry (CMI), University of Namur, 61 rue de Bruxelles, B-5000 Namur, Belgium; E-mail: bao-lian.su@unamur.be*
[d] *Department of Chemistry and Clare Hall, University of Cambridge, Cambridge, CB2 1EW, UK; E-mail: bls26@cam.ac.uk*

† Electronic Supplementary Information (ESI) available: EDX pattern, FT-IR spectra, TG/DSC plots, Nitrogen adsorption-desorption isotherms and some other supplementary Figures. See DOI: 10.1039/x0xx00000x

technique,[18] hydrothermal reaction,[11] microwave-assisted method,[19] thermal decomposition,[20] have been conducted for MnO_2 electrodes in LIBs, the design of uniform porous MnO_2 materials in nanoscale with high monodispersity is still challenging. Therefore, rational design and synthesis of uniform porous MnO_2 nanostructures with high monodispersity and with *in situ* carbon coating for enhanced conductivity can represent a significant step towards commercial MnO_2-based anode materials.

Herein, we report synthesis of walnut-shaped porous MnO_2/carbon nanospheres (P-MO/C-NSs) with a narrow size distribution for high performance LIBs via *in situ* carbonization of amorphous MnO_2 nanospheres prepared by a one-pot solution-phase reaction. Polyvinylpyrrolidone (PVP) plays dual key roles in the reaction system: as the surfactant for morphology control and as the carbon source to form the carbon scaffold along with MnO_2 crystallization. When used as the anode material for LIBs, the walnut-shaped porous nanostructure endows P-MO/C-NSs with high specific capacity, enhanced cycling stability and rate capability through enhanced reaction kinetics.

2. Experimental section

2.1 Material synthesis

All the reactants and solvents are analytical grade and used without any further purification. The preparation of P-MO/C-NSs is very facile. First, 0.474 g of $KMnO_4$, 1.2 g of NH_4HCO_3 and 0.1 g of polyvinylpyrrolidone (PVP) are dispersed in 35 mL distilled water and stirred for 20 min. Subsequently, 70 mL isopropanol is added into the solution and stirred for another 20 min. The purple black solution is then heated to 80 °C with vigorous stirring for 5 h. The obtained brown precipitate is washed with distilled water and ethanol repeatedly and dried at 60 °C for 4 h. Finally, black MnO_2/C powders are obtained by carbonization of the brown precipitate in argon at 300 and 400 °C for 5 h, respectively.

2.2 Material characterizations

X-ray diffraction (XRD) patterns are obtained by a Bruker diffractometer at 40 kV, 40 mA, with Cu Kα radiation (λ=1.54056 Å). The morphology of all the products is observed using a scanning electron microscope (SEM, Hitachi S-4800) equipped with a field-emission gun at 5 kV acceleration voltage. Transmission electron microscopy (TEM), high resolution transmission electron microscopy (HRTEM), scanning transmission electron microscopy (STEM) and energy-dispersive X-ray spectroscopy (EDS) are acquired on a FEI Talos F200X with 200 kV acceleration voltage. The Brunauer-Emmett-Teller (BET) specific surface area of the powders is analyzed in a Micrometrics Tri Star II 3020 liquid nitrogen adsorption-desorption apparatus. Thermogravimetric analysis (TGA) is performed using a Labsys Evo S60/58458 thermal analysis instrument at 5 °C min^{-1} temperature ramping rate in argon. Fourier transform infrared (FT-IR) spectra are recorded on a Bruker Vertex 80 V FT-IR spectrometer using KBr pellet technique in 400-4000 cm^{-1} range. The surface electronic states of Mn, O are analyzed by X-ray photoelectron spectroscope (XPS, VG Multilab 2000). Raman spectra are carried out at room temperature, and the signals are recorded by an Invia Raman Microscope (Invia Microscope, Renishaw, UK) using a 632.8 nm excitation wavelength.

2.3 Electrochemical measurement

The working electrodes are fabricated by using MnO_2 as active materials, conductive carbon black (Super-P) and polyvinylidene fluoride (PVDF) binder in a 70: 20: 10 weight ratio. The slurry is coated on a copper foil and dried in a vacuum oven at 120 °C for 12 h. The average mass loading of the active materials is 1.57 ± 0.05 mg/cm^2. Electrochemical measurements are carried out via CR2025 coin type cell using lithium foils as the counter electrode and the reference electrode, a 1 M solution of $LiPF_6$ in ethylene carbonate (EC)/dimethyl carbonate (DMC) (1:1 w/w) as electrolyte. The cells are assembled in an argon-filled glove-box. Cyclic voltammetry (CV) measurements are carried out using a CHI 660D electrochemical workstation at 0.2 mV s^{-1} sweep rate. Galvanostatic discharge/charge cycling is studied in a potential range of 0.01-3 V vs Li/Li^+ with a multichannel battery testing system (LAND CT2001A). Electrochemical impedance spectra (EIS) are measured with an electrochemical workstation (Autolab PGSTAT 302N) from 100 kHz to 10 mHz.

3. Results and discussions

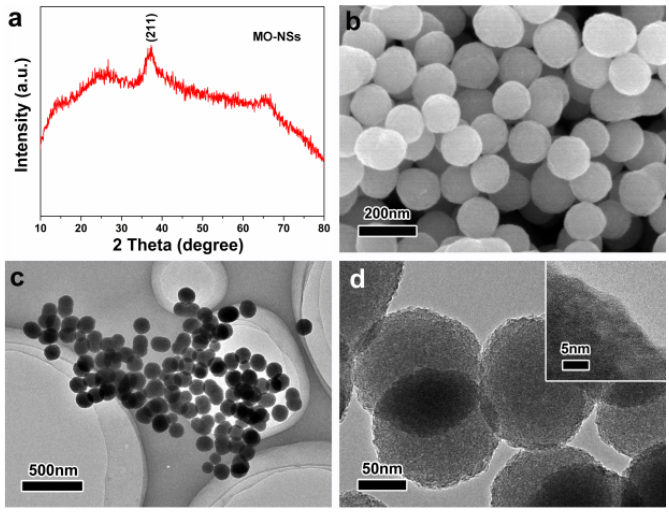

Fig. 1. Characterizations of the as-prepared MO-NSs: (a) typical XRD pattern, (b) SEM image, (c) and (d) TEM images. The inset in (d) is a HRTEM image of the edge of one nanosphere.

XRD is first used to determine the structure of the precursor of MnO_2 nanospheres (designated as MO-NSs) as shown in Fig. 1a. The weak reflections indicate its poor crystallinity (nearly amorphous) and can be indexed to the tetragonal α-MnO_2 (JCPDS no. 44-0141), which consists of 2D edge-shared [MnO_6] octahedra layers (Fig. 2a). EDX analysis shows the presence of K element in the MO-NSs with a K/Mn atomic ratio of ~0.17 (Fig. S1, ESI†). The K^+ cations are expected to be located in the tunnel or interlayer space of α-MnO_2 (Fig.2b).[11, 21] FT-IR (Fig. S2,

ESI†) is carried out to reveal the bonding situation in MO-NSs, which demonstrates the existence of PVP in the amorphous MnO_2 nanospheres. Fig. 1b presents an SEM image of MO-NSs, showing spherical morphology with high uniformity. Size distribution of MO-NSs upon SEM investigation (Fig. S3, ESI†) shows an average diameter of ~150 nm. Fig. 1c-d shows TEM images of the monodispersed MO-NSs nanospheres of 150 nm diameter, consistent with the SEM images. The HRTEM image in Fig. 1d inset reveals the amorphous nature of MO-NSs, again, in good agreement with the XRD analysis.

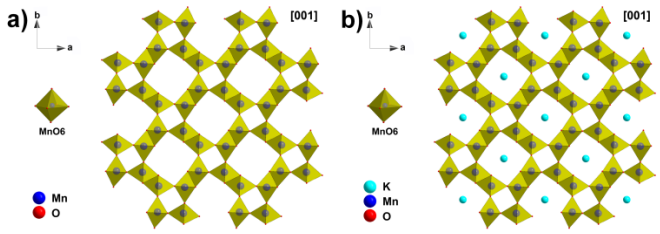

Fig. 2. Crystal structures of α-MnO_2 (a) and as-prepared $K_{0.17}MnO_2$ (KMO) (b) along [001].

We note that PVP plays a key role in the synthesis of MO-NSs. Without PVP, only non-uniform MnO_2 nanoparticles are obtained (Fig. S4, ESI†). In presence of PVP, the product consists of well-dispersed nanospheres with high uniformity (Fig. 1b). It is known that PVP can be used as a surfactant (steric stabilizer) to protect the product from fast agglomeration in the solution-phase for the synthesis of various colloidal particles [22, 23]. Without PVP in the reaction system, the newly formed nanocrystallites tend to quickly agglomerate to reduce their surface energy, resulting in non-uniform nanoparticles (Fig. 3). On the contrary, when PVP is used in the synthesis, it can easily be adsorbed on the newly formed nanocrystallites, acting as a surfactant to prevent the nanoparticles from random growth. In addition, the steric forces due to the adsorbed PVP can keep the nucleated ligands from contacting each other, preventing the particles from fast agglomeration. As the reaction proceeds, the nanocrystallites gradually form a spherical morphology to reduce their surface energy (Fig. 3).

TGA/DSC is then employed to investigate the appropriate calcination temperature of the MO-NSs precursor in argon. There are two weight losses in the TGA plot (Fig. S5, ESI†). The first one at ~200-300 °C corresponds to the decomposition of PVP in MO-NSs and the other in the 480-530 °C temperature range is associated with the phase transformation of MnO_2 to Mn_3O_4. This phase transformation can be further confirmed by the XRD pattern (Fig. S6, ESI†), in which a part of MnO_2 is converted to Mn_3O_4 when the temperature reaches 500 °C. Herein, two temperatures of 300 °C and 400 °C under argon atmosphere are employed to obtain the pure MnO_2 (designated as MO/C-NSs and P-MO/C-NSs, respectively as schemed in Fig. 3).

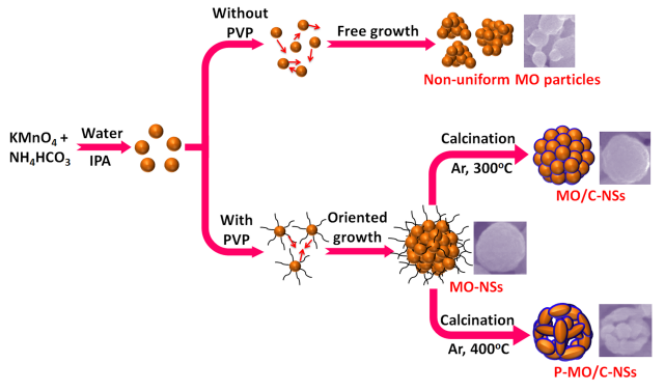

Fig. 3. Schematic illustration of the preparation processes of MO-NSs, MO/C-NSs and P-MO/C-NSs.

Fig. 4a presents the XRD patterns of MO/C-NSs and P-MO/C-NSs. MO/C-NSs exhibit amorphous nature, similar to that of MO-NSs (Fig. 1a), suggesting virtually no crystallization under such a low temperature of 300 °C. After annealing at a higher temperature (400 °C), P-MO/C-NSs deliver sharp peaks of tetragonal α-MnO_2 (JCPDS no. 44-0141). The K element still exists in P-MO/C-NSs with a K/Mn atomic ratio ~0.17 from the EDX result (Fig. 4b), similar to the result of MO-NSs (Fig. S1, ESI†) and MO/C-NSs (Fig. S7, ESI†). Moreover, EDX pattern demonstrates the presence of carbon in MO/C-NSs and P-MO/C-NSs, coming from *in situ* carbonization of PVP in argon. TGA is further employed to determine the carbon contents in the two samples (Fig. S8, ESI†), which displays a carbon content value of 5.62% and 2.71% for MO/C-NSs and P-MO/C-NSs respectively.

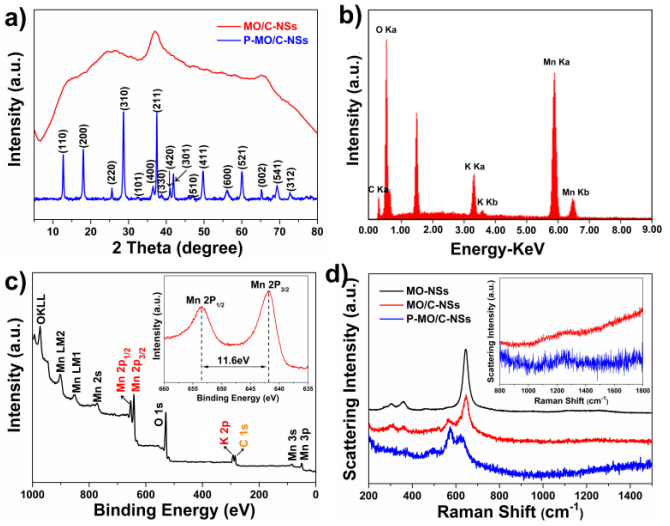

Fig. 4. (a) XRD patterns of MO/C-NSs and P-MO/C-NSs, (b) typical EDX pattern of P-MO/C-NSs, (c) survey XPS spectrum of P-MO/C-NSs and (d) Raman spectra of MO-NSs, MO/C-NSs and P-MO/C-NSs. The inset in (c) is a high resolution XPS of Mn 2p of P-MO/C-NSs and in (d) is enlarged A1g vibration mode of the disordered carbon for MO/C-NSs and P-MO/C-NSs.

XPS measurement is carried out to investigate the oxidation state of Mn and the composition of manganese oxide in P-MO/C-NSs. Survey XPS analysis (Fig. 4c) shows the presence of C and K elements. The K/Mn ratio obtained from the XPS result is ~0.17, in good agreement with the EDX result (Fig. 4b). Fig. 4c inset represents the Mn 2p binding energies of two characteristic peaks at 641.85 and 653.45 eV, corresponding to the Mn $2p_{3/2}$ and Mn $2p_{1/2}$ spin-orbit peaks with a spin-energy separation of 11.6 eV, in good agreement with K-containing

MnO_2,[11, 14, 24] demonstrating mostly +3 and +4 Mn oxidation states. Based on the results of EDX on K/Mn ratio and XPS results, the average oxidation state of Mn is ~+3.83, resulting in the formula $K_{0.17}MnO_2$. The crystal structures of tetragonal α-MnO_2 and $K_{0.17}MnO_2$ are both illustrated in Fig.2, where K^+ cations locate in the tunnel or interlayer space of α-MnO_2 to form the (2 × 2) tunnel structure (Fig. 2b)[11, 21] improving the structural stability during discharge-charge process.

The obtained three α-MnO_2 materials are further characterized by Raman spectroscopy (Fig. 4d). As for MO-NSs, there are three bands at 314, 387 and 647 cm^{-1}, which are assigned to Mn_3O_4 formation during the spectra acquisition because of the local heating of the sample when using 632.8 nm laser at a fixed laser power (17 mW on the sample) with 10 s acquisition time. This is often observed for MnO_2 samples during Raman study.[25, 26] While for MO/C-NSs and P-MO/C-NSs, an additional band locating at 579 cm^{-1} appears. This can be attributed to the Mn-O lattice vibration in MnO_2, which has already been observed in both birnessite-type MnO_2 and α-MnO_2.[27, 28] It is interesting to note that MO/C-NSs are also mostly transformed into Mn_3O_4 via local laser heating, indicating the unstable phase. However, only a part of P-MO/C-NSs is converted to Mn_3O_4 under local laser heating, due to better crystallinity and carbonized surface layer that prevent the sample from easy phase transformation under laser induced heating.[28] In addition, the Raman spectra also demonstrate a weak peak locating at ~1250 cm^{-1} for both MO/C-NSs and P-MO/C-NSs. This corresponds to the A_{1g} vibration mode of the disordered carbon.[29, 30] The intensity of the peak at around 1250 cm^{-1} for P-MO/C-NSs is a little higher than that of MO/C-NSs, indicating better carbonization of P-MO/C-NSs.

SEM and TEM observations are further carried out to investigate the morphology and detailed structure of MO/C-NSs and P-MO/C-NSs. After being annealed at 300 °C, the size and spherical structure of MO/C-NSs are maintained with good monodispersity and uniformity (Fig. 3 and Fig. S9, ESI†). The HRTEM image (Fig. S9b inset, ESI†) reveals the amorphous nature of MO/C-NSs, indicating that the low temperature calcination does not result in further crystallization of the α-MnO_2 structure, in good agreement with the XRD analysis.

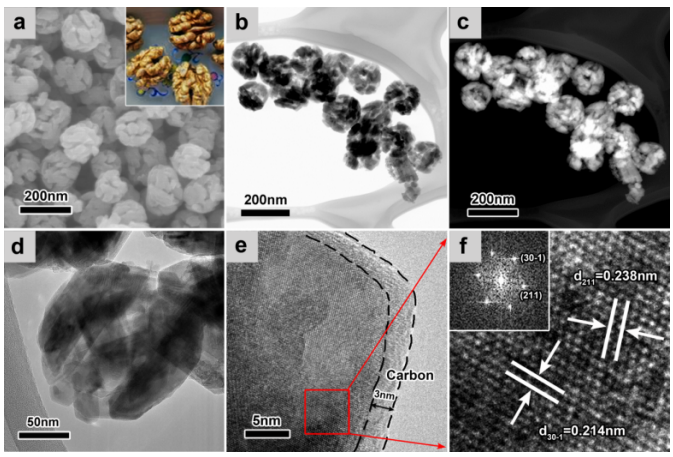

Fig. 5. SEM and TEM characterizations of P-MO/C-NSs: (a) SEM image, (b) TEM image, (c) corresponding HAADF image of (b), (d) TEM image of a single nanosphere and (e-f) HRTEM image. The inset in (a) is photograph of walnuts to highlight the structural similarity of P-MO/C-NSs. The inset in (f) is the corresponding fast Fourier transform (FFT).

After annealing at 400 °C, the sample shows a unique walnut-shaped porous nanosphere structure, constructed from interconnected nanocrystals (Fig. 3 and Fig. 5a). We ascribe this to the combustion of PVP and crystallization of MnO_2 accompanying with the atomic migration.[31] It is worth noting that in spite of the structural transformation, P-MO/C-NSs maintain high monodispersity and uniformity. A typical low magnification TEM image and corresponding high angle annular dark-field (HAADF) image confirm that P-MO/C-NSs are porous nanospheres composed of interconnected nanocrystals (Fig. 5b-c). A high magnification TEM image of a single nanosphere confirms the nanocrystal-constructed nanospheres (Fig. 5d). The HRTEM image in Fig. 5e clearly displays a carbon layer of ~3 nm on the α-MnO_2 crystal surface. Fig. 5f demonstrates well-resolved lattice fringes with an interplanar spacing of 0.238 nm and 0.214 nm, corresponding to the (211) plane and (30-1) plane of tetragonal structure of α-MnO_2, respectively.

TEM element mapping is conducted on a single P-MO/C-NS nanosphere. Fig. 6a shows the dark-field image of the single nanosphere. Fig. 6b-f clearly displays that P-MO/C-NSs are composed of C, Mn, O and K elements with homogeneous distribution among the whole nanosphere. To further demonstrate homogeneous distribution of all elements, electron tomography combining with HAADF is used to reconstruct the 3D morphology. Fig. 6g depicts the reconstructed morphology of one P-MO/C-NS nanosphere, which demonstrates C, Mn, O and K elements being homogeneously distributed in the whole nanosphere. Particularly, Fig. 6h and i present the reconstructed morphology of carbon and K, more clearly revealing homogeneous distribution of C and K elements. The uniformity of K element in P-MO/C-NSs verifies the K^+ cations in the tunnel or interlayer space of α-MnO_2. The nitrogen adsorption-desorption isotherms of MO-NSs, MO/C-NSs and P-MO/C-NSs are also characterized (Fig. S10, ESI†). P-MO/C-NSs exhibit a typical type IV N_2 isotherm with type-H1 hysteresis loops, suggesting the presence of mesopores.[32] The BET specific surface areas of MO-NSs, MO/C-NSs and P-MO/C-NSs are measured to be ~10 m^2 g^{-1}, 11 m^2 g^{-1} and 32 m^2 g^{-1}, respectively. The highest specific surface area of P-MO/C-NSs is attributed to the porous structure as revealed by SEM and TEM observations.

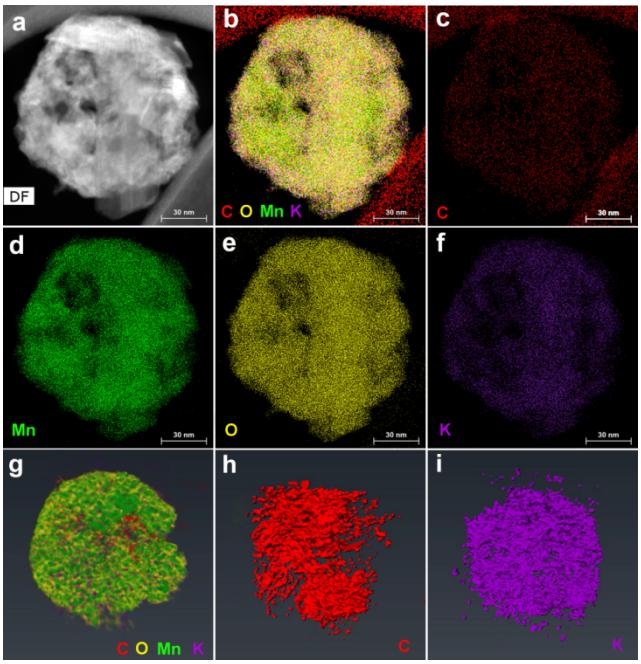

Fig. 6. TEM element mapping images of P-MO/C-NSs: (a) dark-field image, (b) combination of all elements, (c) C, (d) Mn, (e) O and (f) K. (g-i) Tomography reconstruction images of P-MO/C-NSs: (g) combination of all elements, (h) C, (i) K.

Fig. 7a and 7b represent the cyclic voltammetry (CV) curves of the MO/C-NSs and P-MO/C-NSs electrodes measured in the voltage range of 3.0 and 0 V at 0.2 mV s^{-1}. As for the P-MO/C-NSs, upon the first scan, three cathodic peaks appear at 1.1, 0.6 and 0.05 V. These correspond to the reduction of manganese dioxide to metallic manganese (Mn^{4+} to Mn^{2+}, Mn^{2+} to Mn^{0}) as well as the formation of Li_2O and a solid electrolyte interphase (SEI) layer.[24, 33, 34] In the anodic scan of the P-MO/C-NSs electrode, two peaks at 1.2 and 2.4 V are observed. These are attributed to re-oxidation of manganese from Mn^{0} to Mn^{2+} and Mn^{2+} to Mn^{3+}, respectively.[35, 36] Compared to those of P-MO/C-NSs, the measurements of MO/C-NSs lack the two additional peaks at ~1.1 V (cathodic scan) and ~2.4 V (anodic scan), indicating poor kinetics of lithiation/delithiation reactions for the MO/C-NSs electrode.[37] The CV results indicate that P-MO/C-NSs have deeper oxidation state than MO/C-NSs. This is likely due to an enhanced reaction kinetics between the P-MO/C-NSs anode material and electrolyte.

Fig. 7c exhibits the first and second discharge/charge profiles of MO/C-NSs and P-MO/C-NSs at 100 mA g^{-1} current density. Consistent with the two reduction peaks in CV curves, one inclined voltage plateau from 1.25 to 1.0 V and one small inflection between 0.75-0.5 V can be observed for P-MO/C-NSs in the first discharge, ascribed to the reduction of Mn^{4+} to Mn^{2+} and the formation of SEI layer, respectively.[38] The main reaction of lithium and MnO_2 occurs at the long voltage plateau at ~0.20 V related to the reduction of Mn^{2+} to Mn^{0}, in good agreement with the CV analysis. The whole reaction can be depicted as $MnO_2 + 4Li \rightarrow Mn + 2Li_2O$.[39, 40] In the first charge curve, an apparent voltage plateau at ~1.3 V can be observed for both samples, corresponding to the reversible oxidation of Mn^{0} to Mn^{2+} during the anodic process.[33] An additional voltage plateau at ~2.2 V corresponding to the further oxidation from Mn^{2+} to Mn^{3+} can be only observed for P-MO/C-NSs, resulting in higher charge capacity of P-MO/C-NSs than MO/C-NSs. In the second discharge curve, only one voltage plateau around 0.5 V can be observed, suggesting that the lithiation reaction of the second cycle is easier, which is often the feature of a single phase reaction.[41] Further oxidation from Mn^{2+} to Mn^{3+} indicates a deeper conversion reaction occurring during the anodic process. Such deeper conversion reaction is likely caused by the enhanced reaction kinetics owing to the walnut-shaped porous structure, offering full contact between the electrolyte and P-MO/C-NSs electrode material.

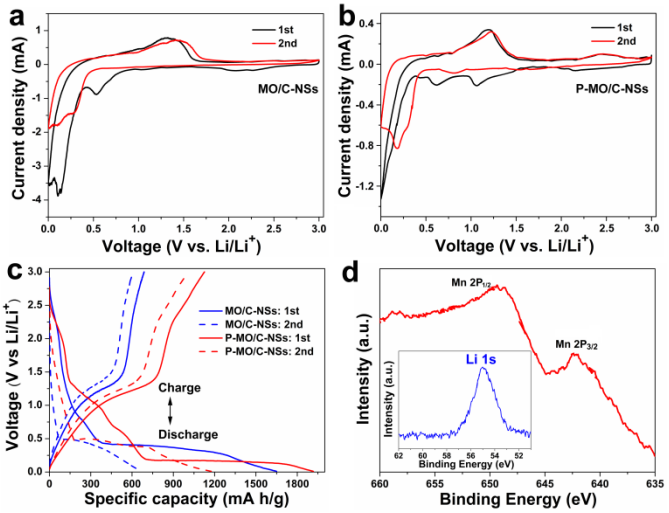

Fig. 7. The electrochemical properties of the MO/C-NSs and P-MO/C-NSs: cyclic voltammograms of (a) MO/C-NSs and (b) P-MO/C-NSs at a scanning rate of 0.2 mV s^{-1}, (c) the first and second discharge/charge profiles of MO/C-NSs and P-MO/C-NSs at 100 mA g^{-1} and (d) XPS spectrum of Mn 2p (the P-MO/C-NSs electrode) after first discharge. The inset in (d) is the XPS of Li 1s spectrum.

XPS is also employed to study the reaction mechanism of the P-MO/C-NSs electrode after lithiation (Fig. 7d). The lithiated electrode displays broader peaks for Mn 2p binding energy with narrow spin-energy separation compared to that of the pristine electrode (Fig. 4c inset), indicating the presence of metallic manganese resulting from the reduction reaction. XPS spectra of Li 1s peak at ~55.2 eV confirms the presence of Li_2O (Fig. 7d inset).[10, 42] The formation of metallic manganese and Li_2O after lithiation reaction confirms that the electrochemical reaction in MnO_2 is based on a conversion reaction.

Fig. 8a compares the cycling performances of MO-NSs, MO/C-NSs and P-MO/C-NSs. The P-MO/C-NSs delivers initial discharge and charge capacities of 1916.2 and 1126.2 mAh g^{-1} at 100 mA g^{-1}, respectively, demonstrating a coulombic efficiency (CE) of 59%. In contrast, the MO-NSs and MO/C-NSs give a low CE of only 5% and 42%, respectively. The improved CE of P-MO/C-NSs is attributed to the more stable surface leading to less side reaction and less irreversible Li consumption.[43] The first irreversible capacity is caused by the

formation of solid electrolyte Interface (SEI) layers and irreversible phase transformation.[44] After calcination, the cycling performance of MO/C-NSs and P-MO/C-NSs significantly improves. This can be ascribed to the good conductivity of MO/C-NSs and P-MO/C-NSs resulting from the *in situ* carbonization process. After 50 cycles of discharge/charge, the P-MO/C-NSs electrodes deliver a much higher reversible specific capacity of ~1176 mA h g^{-1}, close to the maximum theoretical capacity of MnO_2 (1230 mA h g^{-1}). In comparison, MO/C-NSs exhibit poor cycling performance with the specific capacity rapidly decreasing to 181 mA h g^{-1} after 50 cycles. Most importantly, it is observed that the specific capacity of P-MO/C-NSs gradually increases after 25 cycles. This phenomenon may come from the further oxidation of Mn^{2+} to Mn^{3+} in the charging process. Further, the voltage plateau at ~ 2.2 V in the charge profiles of P-MO/C-NSs becomes more and more evident during the cycling process (Fig. 8b), indicating more Mn^{2+} ions are oxidized to Mn^{3+} ions, resulting in an increase in specific capacity. Further oxidation of Mn^{2+} to Mn^{3+} can also be confirmed by the XPS spectrum of P-MO/C-NSs after 50 discharge/recharges (Fig. 8c), in which two peaks of Mn $2p_{3/2}$ and Mn $2p_{1/2}$ are at 642.0 and 653.65 eV, respectively, with a spin-energy separation of 11.65 eV, corresponding to Mn^{3+}.[45, 46] Therefore, compared to MO/C-NSs, P-MO/C-NSs provide enhanced conversion reaction kinetics between the electrolyte and the electrode material, resulting in a deeper conversion reaction during the discharge/charge cycling process. We propose that this enhanced kinetics of P-MO/C-NSs is closely related to its walnut-shaped porous structure and enhanced conductivity due to the better crystallinity and intimate carbon layer, leading to improved cycling performance and increased specific capacity.

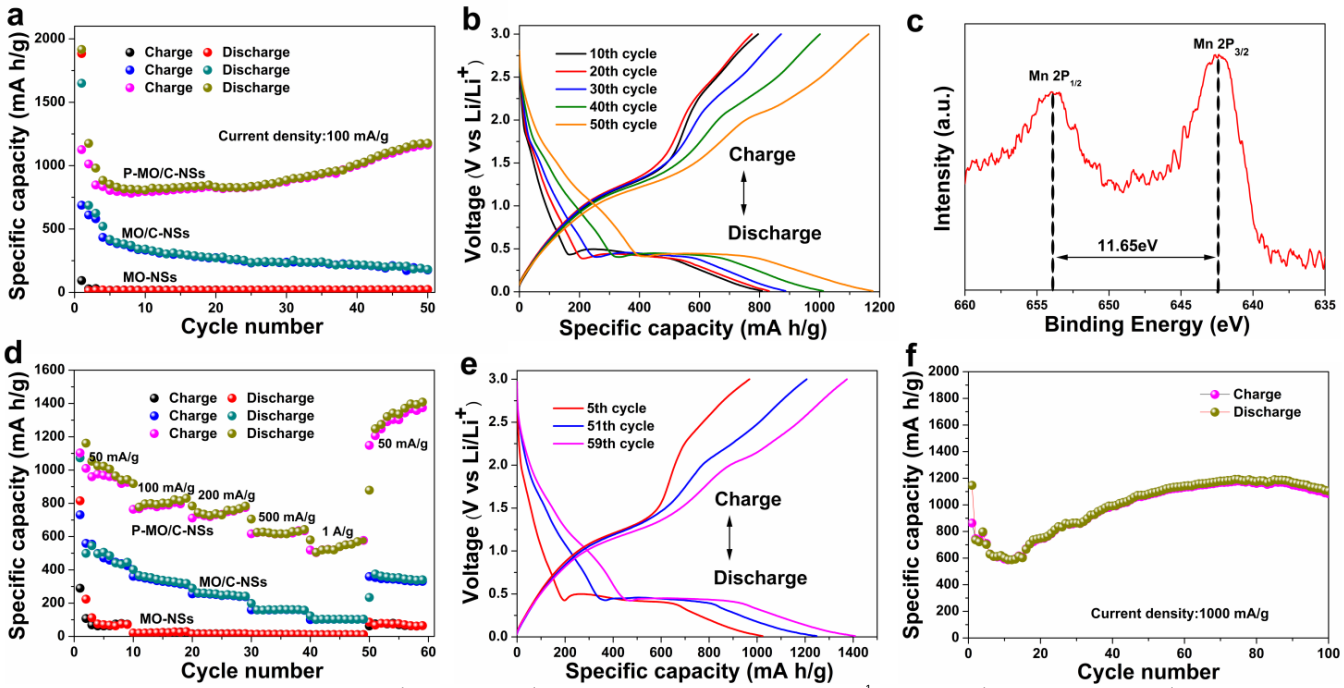

Fig. 8. The electrochemical properties of MO-NSs, MO/C-NSs and P-MO/C-NSs: (a) cycling performance at 100 mA g^{-1}, (b) discharge/charge profiles of P-MO/C-NSs at different cycles, (c) the XPS spectrum of Mn 2p (P-MO/C-NSs) after 50 discharge/recharges, (d) discharge/charge capacities at various current densities, (e) discharge/charge profiles of the rate capability (P-MO/C-NSs) in the 5th, 51th and 59th cycle, respectively and (f) cycling performance of P-MO/C-NSs at 1000 mA g^{-1}.

The representative rate performances of MO-NSs, MO/C-NSs and P-MO/C-NSs are presented in Fig. 8d and Fig. S11 (ESI†). With increase in current density, the P-MO/C-NSs electrode delivers a highly reversible capacity of 960, 800, 730 and 627 mA h g^{-1} at 50, 100, 200 and 500 mA g^{-1} current densities, respectively, demonstrating excellent rate capability. Even at a high current density of 1000 mA g^{-1}, the electrode delivers a high reversible capacity of 540 mA h g^{-1}, higher than the theoretical capacity of graphite (372 mA h g^{-1}). As a comparison, MO-NSs and MO/C-NSs deliver much lower specific capacities (at 50, 100, 200, 500 and 1000 mA g^{-1}, the specific capacities of the two samples are 68/470, 23/335, 16/248, 13/160, 11/101 mA h g^{-1}, respectively). It should be noted that when the current density is reduced back to 50 mA g^{-1}, the specific capacity of P-MO/C-NSs (1407 mA h g^{-1}) is much higher than the initial capacity (976 mA h g^{-1}), and even higher than the theoretical capacity of MnO_2 (1230 mA h g^{-1}). This is most likely due to further deep oxidation of manganese from Mn^{2+} to Mn^{3+} as discussed above. The corresponding discharge/charge profiles are also presented in Fig. 8e, which clearly shows the deeper oxidation at 59th cycle than at 51th cycle due to the enhanced reaction kinetics for specific capacity increase. Further, the reversible growth of pseudocapacitive polymeric gel-like film may partially contribute to the specific capacity, resulting in higher value than the theoretical maximum.[47, 48] Specifically, at the high current density of 1000 mA g^{-1}, the P-MO/C-NSs still show superior cycling performance (Fig. 8f). In spite of initial drop,

from ~12 cycles, the specific capacity increases gradually. After 85 cycles, the specific capacity reaches a maximum high of 1192 mA h g^{-1}, close to the theoretical capacity of MnO_2 (1230 mA h g^{-1}). To the best of our knowledge, this is the highest ever reversible capacity reported for manganese oxides based electrode at such a high current rate. Table S1 (ESI†) lists the electrochemical performance comparison between the P-MO/C-NSs and previously reported MnO_2 materials, which demonstrates the superiority of P-MO/C-NSs for LIBs. The corresponding discharge/charge profile at the 85th cycle shows very good plateaus (Fig. S12, ESI†), similar to the profiles at low current density of 50 mA g^{-1} (Fig. 8e), indicating the low electrochemical polarization and highly enhanced reaction kinetics of P-MO/C-Ns at such a high rate. The high rate capability of P-MO/C-NSs is revealed via the electrochemical impedance spectroscopy (EIS), which shows that the semicircle diameter of P-MO/C-NSs is smaller than those of MO-NSs and MO/C-NSs (Fig. S13, ESI†). This indicates that the charge-transfer process of P-MO/C-NSs at the electrode/electrolyte interface exhibits much more enhanced reaction kinetics than those of MO-NSs and MO/C-NSs owing to its walnut-shaped porous structure with intimate carbon coating.

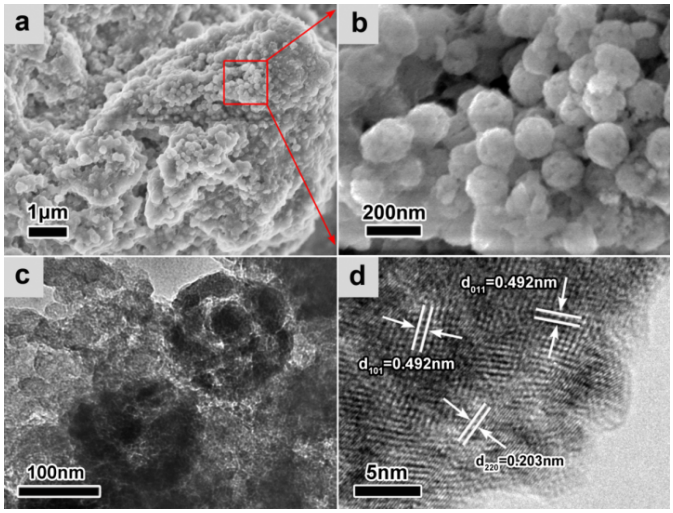

Fig. 9. The *ex situ* SEM and TEM characterizations of the P-MO/C-NSs electrode after 50 discharge-recharges at 1000 mA g^{-1}: (a-b) SEM images, (c) TEM image and (d) HRTEM image.

To further understand the Li^+ storage property and the structural stability of the P-MO/C-NSs anode material, post-mortem investigations on the anode material after 50 discharge-charge cycles at 1000 mA g^{-1} are carried out by SEM, TEM and HRTEM (Fig. 9). We find that after 50 discharge/charge cycles, the monodispersity and uniformity of P-MO/C-NSs nanospheres are perfectly preserved without any morphological alterations of the porous framework. This demonstrates the robustness of the walnut-shaped porous MnO_2/C materials, making them very effective electrode materials for high rate applications in LIBs. The inter-planar spacings of the lattice fringes of the *ex situ* electrode material are measured to be 0.492 nm, 0.492 nm and 0.203 nm, which correspond to the (101), (011) and (220) planes of Mn_3O_4 (JCPDS no. 80-0382) respectively, further confirming the formation of Mn^{3+} after 50 discharge-charge cycles due to the enhanced reaction kinetics.

The above results and analyses show that the walnut-shaped porous P-MO/C-NS electrode materials have several advantages, including high specific capacity, improved cycle performance and good rate capability as shown in Fig. 10. The mesoporous nature of the P-MO/C-NS electrode facilitates good contact with electrolyte and further promotes the transportation of lithium ions, effectively buffer the structural strain and volume changes in the anode during repeated electrochemical reactions, which effectively relieves pulverization and improves the cycling performance and rate capability. On the other hand, the presence of intimate carbon layer on the MnO_2 nanocrystallites in the walnut-shaped P-MO/C-NS electrode due to *in situ* carbonization can greatly enhance the conductivity of the electrode material. The synergy of the walnut-shape porous structure and intimate carbon layer covering the MnO_2 nanocrystallites can enhance the kinetics of conversion reactions, resulting in high specific capacity and high rate capability of the P-MO/C-NSs anode material.

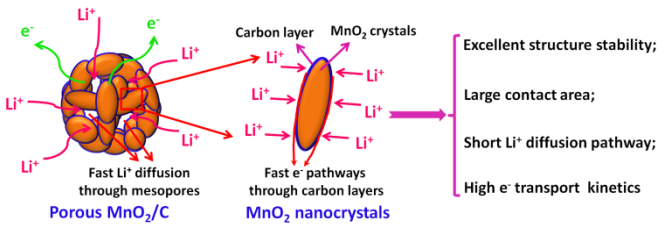

Fig. 10. Schematic illustration of lithium insertion mechanism in P-MO/C-NSs.

4. Conclusions

We have developed an in situ strategy to fabricate highly monodispsersed walnut-shaped porous MnO_2/carbon nanospheres (P-MO/C-NSs). Use of polyvinylpyrrolidone (PVP) is very important for both morphology control and carbon scaffold formation along with the crystallization of MnO_2. When evaluated as anode material for LIBs, P-MO/C-NSs, with the carbon coating on the nanocrystallite surface exhibit very high reversible capacity (1176 mA h g^{-1} at 100 mA g^{-1}), good cycling stability and excellent rate capability (540 mA h g^{-1} at 1 A g^{-1}). The unique nanostructure of P-MO/C-NSs provides large electrode-electrolyte contact areas, short Li^+ ion transport paths, low charge transfer resistance and superior structural stability, resulting in enhanced reaction kinetics for superior electrochemical performance. This work highlights that designing conversion electrodes based on carbon coated porous nanocomposites with a stable electrochemical system during discharge/charge cycling is a very promising approach to achieve superior lithium-storage properties.

Acknowledgements

This work is realized in the frame of a program for Changjiang Scholars and Innovative Research Team (IRT_15R52) of

Chinese Ministry of Education. B. L. Su acknowledges the Chinese Central Government for an "Expert of the State" position in the Program of the "Thousand Talents" and a Life Membership at the Clare Hall, Cambridge and the financial support of the Department of Chemistry, University of Cambridge. Y. Li acknowledges Hubei Provincial Department of Education for the "Chutian Scholar" program. T. Hasan acknowledges funding from the Royal Academy of Engineering (Graphlex) and an Impact Acceleration Award (GRASS). This work is also financially supported by the National Science Foundation for Young Scholars of China (No. 21301133 and 51302204), International Science & Technology Cooperation Program of China (2015DFE52870) and and Self-determined and Innovative Research Funds of the SKLWUT (2015-ZD-7). The authors also would like to thank Dr. Bin-Jie Wang from Shanghai Nanoport (FEI, Shanghai) for TEM analysis, and thank Hang Ping from Wuhan University of Technology for the TGA/DSC tests.

Notes and references

1. Y. K. Sun, Z. Chen, H. J. Noh, D. J. Lee, H. G. Jung, Y. Ren, S. Wang, C. S. Yoon, S. T. Myung and K. Amine, *Nat. Mater.*, 2012, **11**, 942.

2. B. L. Ellis, P. Knauth and T. Djenizian, *Adv. Mater.*, 2014, **26**, 3368.

3. L. Mai, X. Tian, X. Xu, L. Chang and L. Xu, *Chem. Rev.*, 2014, **144**, 11828.

4. Y. S. Hu, R. Demir-Cakan, M. M. Titirici, J. O. Müller, R. Schlögl, M. Antonietti and J. Maier, *Angew. Chem. Int. Ed.*, 2008, **47**, 1645.

5. Y. Xiao, S. Liu, F. Li, A. Zhang, J. Zhao, S. Fang and D. Jia, *Adv. Funct. Mater.*, 2012, **22**, 4052.

6. Y. Ma, C. Fang, B. Ding, G. Ji and J. Y. Lee, *Adv. Mater.*, 2013, **25**, 4646.

7. J. M. Jeong, B. G. Choi, S. C. Lee, K. G. Lee, S. J. Chang, Y. K. Han, Y. B. Lee, H. U. Lee, S. Kwon and G. Lee, *Adv. Mater.*, 2013, **25**, 6250.

8. M. Reddy, G. Subba Rao and B. Chowdari, *Chem. Rev.*, 2013, **113**, 5364.

9. C. X. Guo, M. Wang, T. Chen, X. W. Lou and C. M. Li, *Adv. Energy Mater.*, 2011, **1**, 736.

10. A. L. M. Reddy, M. M. Shaijumon, S. R. Gowda and P. M. Ajayan, *Nano Lett.*, 2009, **9**, 1002.

11. L. Li, C. Nan, J. Lu, Q. Peng and Y. Li, *Chem. Commun.*, 2012, **48**, 6945.

12. J. Deng, L. Chen, Y. Sun, M. Ma and L. Fu, *Carbon*, 2015, **92**, 177.

13. Y. Hou, Y. Cheng, T. Hobson and J. Liu, *Nano Lett.*, 2010, **10**, 2727.

14. H. Xia, M. Lai and L. Lu, *J. Mater. Chem.*, 2010, **20**, 6896.

15. X. Gu, L. Chen, Z. Ju, H. Xu, J. Yang and Y. Qian, *Adv. Funct. Mater.*, 2013, **23**, 4049.

16. F. Jiao and P. G. Bruce, *Adv. Mater.*, 2007, **19**, 657.

17. Y. Li, Z. Y. Fu and B. L. Su, *Adv. Funct. Mater.*, 2012, **22**, 4634.

18. A. Yu, H. W. Park, A. Davies, D. C. Higgins, Z. Chen and X. Xiao, *J. Phys. Chem. Lett.*, 2011, **2**, 1855.

19. K. Chen, Y. Dong Noh, K. Li, S. Komarneni and D. Xue, *J. Phys. Chem. C*, 2013, **117**, 10770.

20. J. Zhao, Z. Tao, J. Liang and J. Chen, *Cryst. Growth Des.*, 2008, **8**, 2799.

21. W. M. Chen, L. Qie, Q. G. Shao, L. X. Yuan, W. X. Zhang and Y. H. Huang, *ACS Appl. Mater. Interfaces*, 2012, **4**, 3047.

22. Y. Xiong, I. Washio, J. Chen, H. Cai, Z. Y. Li and Y. Xia, *Langmuir*, 2006, **22**, 8563.

23. J. Zhang, H. Liu, Z. Wang and N. Ming, *Adv. Funct. Mater.*, 2007, **17**, 3295.

24. M. Kundu, C. C. A. Ng, D. Y. Petrovykh and L. Liu, *Chem. Commun.*, 2013, **49**, 8459.

25. G. Tao, F. Helmer and N. Poul, *Anal. Chim. Acta*, 2009, **648**, 235.

26. E. Widjaja and J. T. Sampanthar, *Anal. Chim. Acta*, 2007, **585**, 241.

27. Y. K. Hsu, Y. C. Chen, Y. G. Lin, L. C. Chen and K. H. Chen, *Chem. Commun.*, 2010, **47**, 1252.

28. J. Luo, H. T. Zhu, H. M. Fan, J. K. Liang, H. L. Shi, G. H. Rao, J. B. Li, Z. M. Du and Z. X. Shen, *J. Phys. Chem. C*, 2008, **112**, 12594.

29. S. Z. Huang, Y. Cai, J. Jin, J. Liu, Y. Li, Y. Yu, H. E. Wang, L. H. Chen and B. L. Su, *Nano Energy*, 2015, **12**, 833.

30. A. Ferrari and J. Robertson, *Phys. Rev. B*, 2000, **61**, 14095.

31. S. Z. Huang, Y. Cai, J. Jin, Y. Li, X. F. Zheng, H. E. Wang, M. Wu, L. H. Chen and B. L. Su, *J. Mater. Chem. A*, 2014, **2**, 14099.

32. A. Vu, Y. Qian and A. Stein, *Adv. Energy Mater.*, 2012, **2**, 1056.

33. H. Lai, J. Li, Z. Chen and Z. Huang, *ACS Appl. Mater. Interfaces*, 2012, **4**, 2325.

34. T. Yang, T. Qian, M. Wang, J. Liu, J. Zhou, Z. Sun, M. Chen and C. Yan, *J. Mater. Chem. A*, 2015, **3**, 6291.

35. S. Z. Huang, J. Jin, Y. Cai, Y. Li, H. Y. Tan, H. E. Wang, G. Van Tendeloo and B. L. Su, *Nanoscale*, 2014, **6**, 6819.

36. J. Yue, X. Gu, L. Chen, N. Wang, X. Jiang, H. Xu, J. Yang and Y. Qian, *J. Mater. Chem. A*, 2014, **2**, 17421.

37. Y. Sun, X. Hu, W. Luo, F. Xia and Y. Huang, *Adv. Funct. Mater.*, 2013, **23**, 2436.

38. Y. Li, Q. Zhang, J. Zhu, X.-L. Wei and P. K. Shen, *J. Mater. Chem. A*, 2014, **2**, 3163.

39. Y. Wang, Z. J. Han, S. F. Yu, R. R. Song, H. H. Song, K. Ostrikov and H. Y. Yang, *Carbon*, 2013, **64**, 230.

40. K. Chen, Y. Dong Noh, K. Li, S. Komarneni and D. Xue, *J. Phys. Chem. C*, 2013, **117**, 10770.

41. J. Gao, M. A. Lowe and H. D. Abruna, *Chem. Mater.*, 2011, **23**, 3223.

42. D. Wang, Y. Zhao, X. Xu, M. H. Kalele, M. Yan, Q. An, X. Tian, J. Xu, L. Qu and L. Mai, *Nanoscale*, 2014, **6**, 8124.

43. R. Yi, F. Dai, M. L. Gordin, S. Chen and D. Wang, *Adv. Energy Mater.*, 2013, **3**, 295.

44. P. Poizot, S. Laruelle, S. Grugeon, L. Dupont and J. Tarascon, *Nature* 2000, **407**, 496.

45. H. Cao, X. Wu, G. Wang, J. Yin, G. Yin, F. Zhang and J. Liu, *J. Phys. Chem. C*, 2012, **116**, 21109.

46. J. F. Moulder, W. F. Stickle, P. E. Sobol and K. D. Bomben, *Handbook of X-ray photoelectron spectroscopy*. Perkin Elmer Eden Prairie, MN: 1992; Vol. 40.

47. Q. Hao, J. Wang and C. Xu, *J. Mater. Chem. A*, 2014, **2**, 87.

48. G. Zhou, D. W. Wang, F. Li, L. Zhang, N. Li, Z. S. Wu, L. Wen, G. Q. Lu and H. M. Cheng, *Chem. Mater.*, 2010, **22**, 5306.

